ACADÉMIE
DES SCIENCES
INSTITUT DE FRANCE

Comptes Rendus

Mécanique

Malo Valmalle, Kim Widell, Risto Ilola and Sven Bossuyt

DIC Analyses and Parameter Calibration of a Strain Aging Sensitive Ductile Cast Iron

CENTRE
MERSENNE

Research article / *Article de recherche*

DIC Analyses and Parameter Calibration of a Strain Aging Sensitive Ductile Cast Iron

Malo Valmalle *, a, b, **Kim Widell** a, **Risto Ilola** a **and Sven Bossuyt** ◉, a

a Aalto University, Department of Mechanical Engineering, Espoo, Finland

b ENS Paris-Saclay, DGM–Department of Mechanical Engineering, Gif-sur-Yvette, France

E-mails: malo.valmalle@ens-paris-saclay.fr (M. Valmalle), kim.widell@aalto.fi (K. Widell), risto.ilola@aalto.fi (R. Ilola), sven.bossuyt@aalto.fi (S. Bossuyt)

Abstract. In the present work, the mechanical response of strain aging sensitive ductile cast iron was studied when subjected to uniaxial tension in temperatures ranging from 20°C up to 300°C. Digital Image Correlation (DIC) was used to measure the strain localization patterns due to dynamic strain aging. A constitutive law based on the Kubin–Estrin–McCormick model (KEMC) was used to model the behavior of the ductile cast iron in temperatures ranging from 20° up to 300°. The displacement fields were successfully measured and the strain localization patterns were observed. These measurements were employed to calibrate the parameters of the constitutive law. Numerical simulations are shown to be in agreement with experimental measurements at the macroscopic scale.

Keywords. Digital Image Correlation (DIC), Dynamic Strain Aging, Plasticity, FEM simulation, Ductile Cast Iron.

1. Introduction

In the KBS-3 method of long-term geological disposal of spent nuclear fuel, the load-bearing inserts of the canisters are to be manufactured from ferritic nodular Ductile Cast Iron (DCI) grade EN-GJS-400-15U. Although this material has been extensively studied for the purpose of long term disposal [1, 2] no studies have considered that at such long timescales Dynamic Strain Aging and the concomitant Portevin–Le Chatelier (PLC) effect could occur in this cast iron at relatively low temperatures. More broadly speaking no models have been proposed and successfully identified yet to describe Dynamic Strain Aging (DSA) and Static Strain Aging (SSA) in cast irons.

The most noticeable features of the PLC effect are serrated flow and propagating plastic strain localisation band. Such features are observed during tensile tests in many industrial alloys within a given range of temperatures and strain rates. It has been observed in nickel-titanium alloys, in alloys containing substitutional atoms like Al-Cu alloys [3–5], Al-Mg alloys [6–8] or involving interstitial atoms like carbon in steels [9, 10]. It has also been reported in nickel [11, 12] and

---

* Corresponding author.

titanium-based [13] alloys. The PLC effect is characteristically associated with a negative strain rate sensitivity of the flow stress, meaning that when the applied strain rate increases the flow stress decreases. Other changes in mechanical properties have been reported in combination with the PLC effect like the loss of ductility and toughness.

The PLC effect is caused at a microscopic scale by DSA, namely the interaction between the solutes atoms and the mobile dislocations. The underlying mechanism being the pinning of dislocations by solute atoms when the diffusion and dislocation motion are taking place at similar rates. As such DSA is active for a combination of temperature and strain rates inherent to the alloy composition. The KEMC model proposed by McCormick [14] and Kubin and Estrin [15] was successfully used to model both DSA and SSA for numerous alloys previously cited [3–13]. This model takes into account the physical origin of the strain aging, i.e. the pinning of dislocations by solute atoms, by the introduction of an additional internal variable called the aging time [16]. Nevertheless until now this model has never been used to model the strain aging behavior of cast irons at temperatures relevant to their use.

This work aims to model the mechanical behavior of the Ductile Cast Iron in the temperature range 20-300 °C in a manner that can predict the strain rate localization phenomena observed experimentally at the higher end of that range. For reliable identification of all the model parameters, the experimental data should span conditions where the dynamic strain aging phenomena do occur and conditions where they do not.

The first part presents the experimental observations of tensile tests performed at two different strain rates in a large temperature range (20-300 °C). 2D Digital Image Correlation (2D DIC) was used for full-field measurements of the localized deformations. In a second part the KEMC constitutive model is introduced. The parameters of this model are then identified using the tensile test data and information from the literature. The identification procedure is based on volume element and full-field simulations. The volume element simulations capture the overall mechanical behavior at each temperature for both strain rates, including the negative strain rate sensitivity in the DSA domain. Finite element modeling of the tensile tests is then required to verify if the strain rate localization is correctly depicted by the parameters compared to the full-field experimental results. Lastly the results and methods are discussed for future work.

2. Experimental procedure

2.1. *Material*

The material used in the present study is a Ductile Cast Iron used by Posiva and SKB in their spent nuclear fuel repositories. The material was extracted from a canister insert (insert I73) obtained by casting and produced for Posiva Oy, Finland. The grade of this specific cast iron is EN-GJS-400-15U. The composition of this cast iron is given in Table 1.

Table 1. Material composition (in wt.%)

C%	Si%	Mn%	P%	Mg%	S%	Cu%
3.48	2.48	0.22	0.01	0.04	0.004	0.02

2.2. *Tensile tests*

The tensile tests were performed at two nominal strain rates (10^{-2}s^{-1} and 10^{-4}s^{-1}) and at five different temperatures ranging from 20°C to 300°C, thus sampling the temperature dependence

of the strain rate sensitivity of the material. Cylindrical specimens with a diameter of 9mm and a gauge length of 54mm were loaded in a 100kN servo-hydraulic tensile test machine with water-cooled grips. The gauge section of the specimens was heated with cartridge heaters placed in two purpose-built heater blocks clamped onto the specimens, one above and one below the gauge section. Independent temperature controllers regulated the power to the heating elements based on the temperatures measured by separate thermocouples welded to the specimen at each end of the gauge section. Full-field strain measurements were obtained from 2D DIC calculations. In order to maintain the prescribed strain rate during the plastic part of the deformation the displacement speed of the crosshead was imposed.

No Lüders peak and plateau were observed, even though in the recent study of static strain aging in this material that led to the current work, Lüders behavior was observed at room temperature after pre-straining [17]. PLC instabilities were observed in the range from 150°C to 300°C, depending on applied the strain rate. The elongation to failure A_u and ultimate strength R_m reached in each of the tests carried out are summarized in Table 2.

The first observations from the tensile tests are made by calculating the strain rate sensitivity (SRS) coefficient S defined as:

$$S = \frac{\sigma_2 - \sigma_1}{ln(\dot{E}_2) - ln(\dot{E}_1)} \tag{1}$$

Where σ_1 and σ_2 are the flow stresses at a specified strain taken from smoothed engineering stress-strain curve for the prescribed strain rates $\dot{E}_1$ and $\dot{E}_2$, respectively. For each tested temperature S was measured at 4% strain (Figure 1).
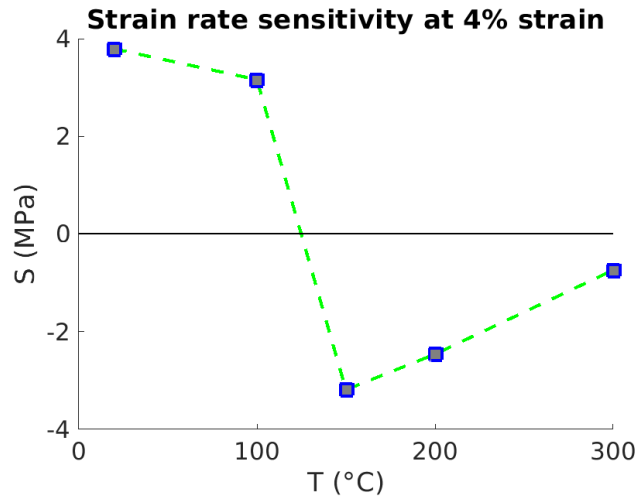

Figure 1. Strain rate sensitivity measured at 4% strain as function of temperature for strain rates between $10^{-2}s^{-1}$ and $10^{-4}s^{-1}$.

The values reveal a strain rate sensitivity drop due to DSA in the 100-300°C temperature range, whereas in the "usual" behavior S would be expected to monotonically increase with temperature. The minimum value of S observed in this work is -3.2 MPa at 150°C. Compared to other studies done on steels [9] the drop of SRS is much more abrupt, highlighting a much faster change of behavior.

Table 2. Mechanical test outcomes.

	$\dot{E}(s^{-1})$	20°C	100°C	150°C	200°C	300°C
A_u(%)	10^{-4}	6.8	8.2	5	9.1	4.3
	10^{-2}	8.6	6.9	4.9	6	6.1
R_m(MPa)	10^{-4}	398	359	340	356	326
	10^{-2}	372	357	324	339	337

2.3. *2D DIC monitoring and fracture observations*

Images were taken at a frequency of 20 Hz during the tests with an applied strain rate of $\dot{E} = 10^{-2}s^{-1}$ and 0.5 Hz during the test with an applied strain rate of $\dot{E} = 10^{-4}s^{-1}$. 2D DIC calculations were performed using the Correli 3.0 framework [18] for each test to capture full field measurements. The region of interest (ROI) was a patch along the gauge length (see Figure 2b). For each test the calculations converged properly with a convergence criterion of 10^{-7} upon the displacement with the analyis parameters shown in Table 6. The displacement and strain noise floors in both directions computed as the maximum values (element wise) of displacement and strain for a series of 20 images of the specimen in the reference configuration are also shown in Table 6.
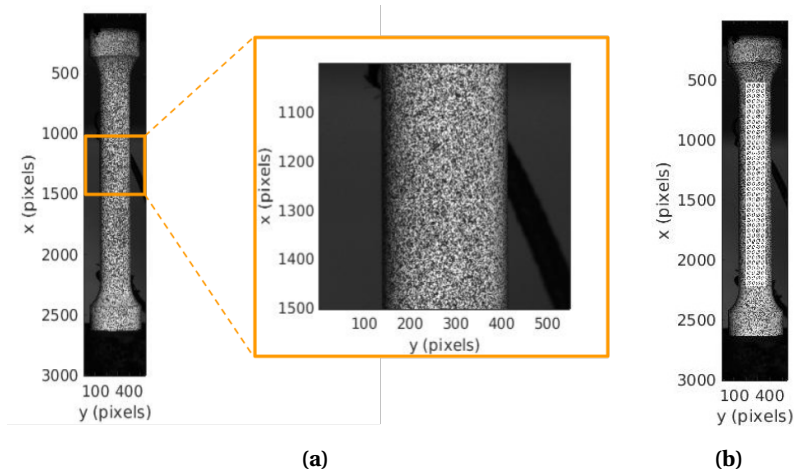

Figure 2. Example of image used for 2D DIC and a closeup on the spray painted pattern (a), T3 mesh used for global 2D DIC (b).

The measured displacement fields were used to retrieve strain/stress curves for the optimization process by means of a virtual extensometer. This virtual extensometer retrieved the displacement at both ends of the ROI to compute the strain along the gauge length. The strain floor of this virtual extensometer, computed as the maximum value of strain obtained for a series of 20 images of the specimen in the reference configuration was of 1.6×10^{-5}. The maximum apparent strain due to out-of-plane displacement (computed at 10% strain with the pinhole camera model) was of the order of 10^{-4} and as such deemed negligible. To visualize the plastic strain rate field $\dot{p}$ the numerical derivative of the total strain field along the gauge length was taken at each time step for each test, and normalized relative to the overall applied strain rate $\dot{E}$. In the range where band localization phenomena were observed, the elastic strain rate estimated from the change in the

load signal and the Young modulus and cross sectional area of the specimen was found negligible compared to the plastic strain rate. For each test the time evolution of this spatial strain rate profile was then displayed in a color plot with a color map indicating the normalized strain rate magnitude. The horizontal color plot coordinates correspond to the time in s of acquisition, and the vertical color plot coordinates X to the vertical distance in mm from the bottom of the ROI where the plastic strain rate $\dot{p}$ was calculated. As such the resolution of the colormap along the vertical direction corresponds to the 2D DIC discretization along the gauge length (see Figure 2) and the resolution along the horizontal direction corresponds to the number of images used for the 2D DIC. The results are shown in Figures 3, 4 and 5.
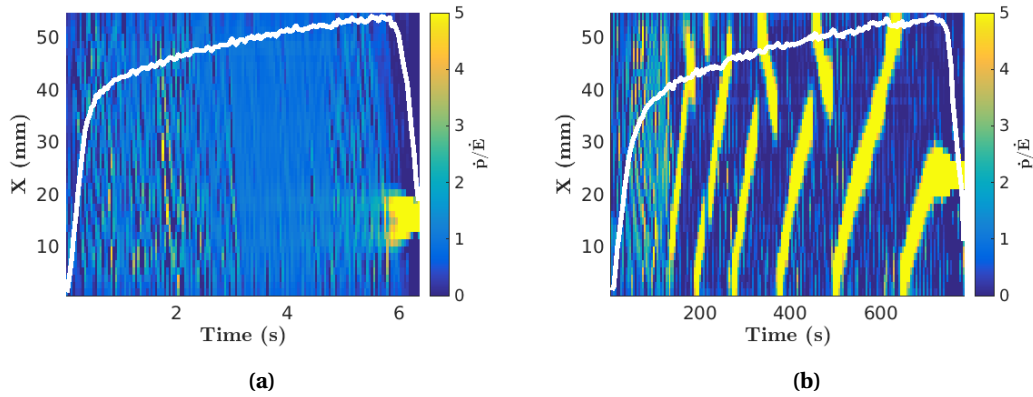

Figure 3. Spatio-temporal graphs of the experiments at 150°C at (a) $\dot{E} = 10^{-2}s^{-1}$ and (b) $\dot{E} = 10^{-4}s^{-1}$.
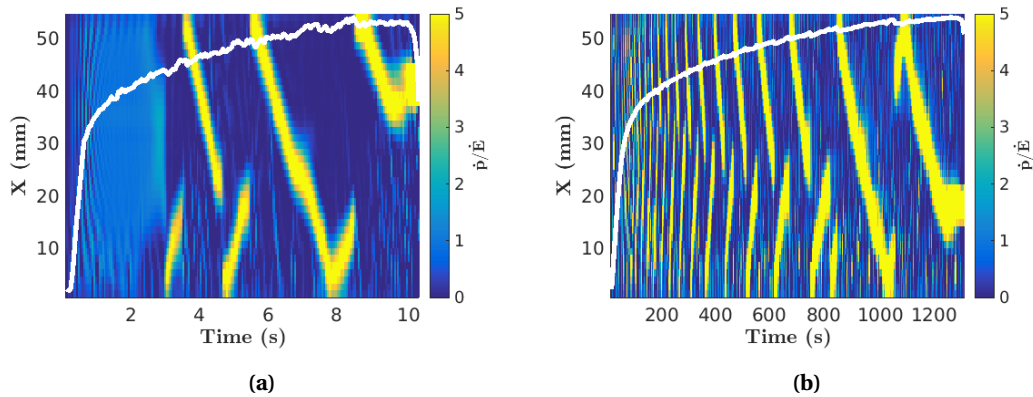

Figure 4. Spatio-temporal graphs of the experiments at 200°C at (a) $\dot{E} = 10^{-2}s^{-1}$ and (b) $\dot{E} = 10^{-4}s^{-1}$.
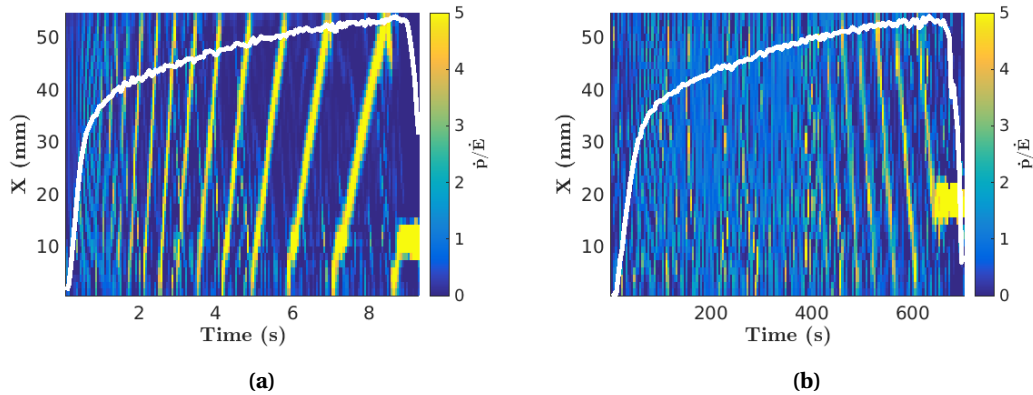
Figure 5. Spatio-temporal graphs of the experiments at 300°C at (a) $\dot{E} = 10^{-2}s^{-1}$ and (b) $\dot{E} = 10^{-4}s^{-1}$.

The PLC effect is clearly observed for a strain rate of $\dot{E} = 10^{-4}s^{-1}$ at a temperature of 150°C (Figure 3b), for both strain rates at a temperature of 200°C (Figures 4a, 4b), and for a strain rate of $\dot{E} = 10^{-2}s^{-1}$ at a temperature of 300°C (Figure 5a). The shape of serrations is significantly different from one test to another. This difference is thought to be the result of the microstructure of the cast iron interfering with the DSA. It is worth mentioning that when DSA is active rupture is always starting inside a localisation band. Since the fracture surfaces did not show any macroscopic salient differences like slant fracture in the DSA domain, SEM observations were performed to check if any differences were to be observed at a microscopic scale. Examples of fracture surfaces of the tests at 20°C and 150°C are visible in Figure 6.
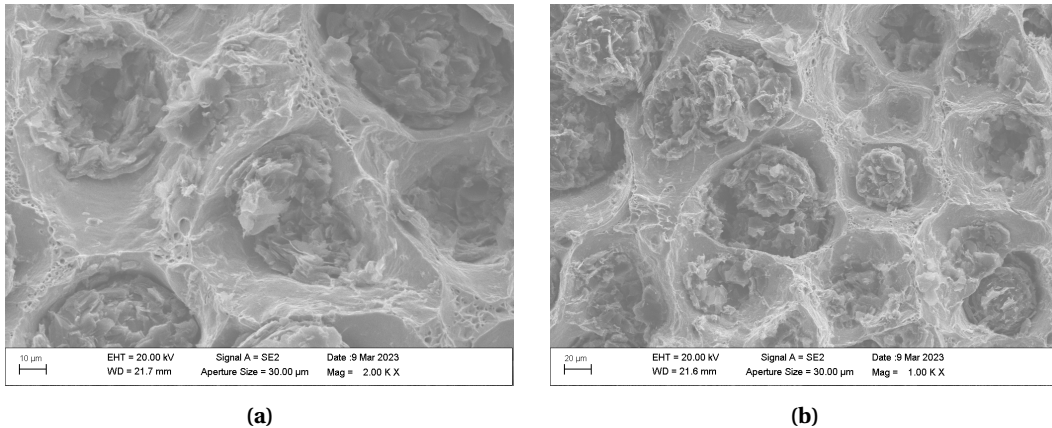

Figure 6. SEM observations of fracture surfaces for the tests at at (a) 20°C $\dot{E} = 10^{-2}s^{-1}$ and (b) 150°C at $\dot{E} = 10^{-4}s^{-1}$.

A typical fracture surface is shown in Figure 6a which shows clearly the flat decohesion areas of the graphite-ferrite interphase and small dimples in the ferrite matrix between them. The DSA behavior did not show any difference in the fracture surfaces. Some evidence of oxide layer formation at 300°C was also observed. In macroscopic investigation the fracture surfaces were smoother and there were less ridges with the lower strain rates. Reduction of area values

calculated from the cross section macrographs were <10%. The values were slightly higher with the higher strain rate for all test temperature, but the differences were small.

3. Constitutive model for strain aging

The DSA phenomenon results from the diffusion of solute atoms like carbon to dislocations temporarily arrested at obstacles like forest dislocations [15]. A constitutive model can represent the contribution of strain aging to the flow stress by taking into account the time dependence of the pinning process and introducing aging time kinetics [16]. The strain aging constitutive model proposed by Zhang et al. [19] is used and modified in this study.

The contribution of strain aging is introduced in the yield function of an elastic-viscoplastic model. This contribution is introduced with an additional internal variable. The stress $\boldsymbol{\sigma}$ is computed from the total strain $\boldsymbol{\varepsilon}$ and the plastic strain $\boldsymbol{\varepsilon}^p$ using Hooke's law with $\underset{\sim}{\boldsymbol{C}}$ the elasticity tensor that is here assumed isotropic with Young Modulus 168 GPa and Poisson coefficient 0.27. (Eq. (2)).

$$\boldsymbol{\sigma} = \underset{\sim}{\boldsymbol{C}}\left(\boldsymbol{\varepsilon} - \boldsymbol{\varepsilon}^p\right) \tag{2}$$

The plastic strain is taken normal to the yield function $f(\boldsymbol{\sigma})$, and the equivalent plastic strain rate follows an hyperbolic sine thermal activation law (Eq. (3)).

$$\dot{\boldsymbol{\varepsilon}}^p = \dot{p}\frac{\partial f}{\partial \boldsymbol{\sigma}} \quad ; \quad \dot{p} = \dot{\varepsilon}_0 \exp\left(-\frac{E_a}{k_b T}\right) \sinh\left(\frac{V_a \langle f(\boldsymbol{\sigma}) \rangle}{k_b T}\right) \tag{3}$$

$$\langle f \rangle = f \quad \text{if} \quad f \geq 0 \quad \text{and} \quad \langle f \rangle = 0 \quad \text{otherwise}$$

Where T is temperature in K, k_b is the Boltzmann constant and $\dot{\varepsilon}_0$, E_a, V_a are respectively a normalization strain rate, the activation energy and the activation volume of the physical mechanisms of plasticity. The yield function $f(\boldsymbol{\sigma})$ is based on a von Mises criterion with an isotropic hardening.

$$f(\boldsymbol{\sigma}) = J_2(\boldsymbol{\sigma}) - R(p) - R_a(p, t_a) \tag{4}$$

Where $J_2(\boldsymbol{\sigma})$ is the second invariant of the stress tensor deviator. The strain hardening term $R(p)$ defined in Eq. (5) was modified from that used in other studies using this type of model, which deal mostly with steels [9, 10]. Since the yielding is much more progressive in cast iron than in steels the exponential hardening term was replaced by a power law, resulting in much better agreement with the experimental results.

$$R = Qp^b + Hp + R_0 \tag{5}$$

Thus, the strain hardening term is composed of a power law term with the parameters Q and b, of a linear hardening term with its slope H and a "microscopic yield stress" R_0 corresponding to the yield stress that would be measured if all the dislocations of the same cast iron were unpinned. The contribution of strain aging to the hardening is introduced as a second hardening term $R_a(p, t_a)$ governed by the cumulative equivalent plastic strain p and a new internal variable t_a, the aging time. This additional term is also assumed to be isotropic and is defined in Eq. (6).

$$R_a(p, t_a) = P_1 C_s(p, t_a) \quad \text{with} \quad C_s = 1 - \exp\left(-P_2 p^\alpha t_a^n\right) \tag{6}$$

The strain aging contribution R_a is proportional to the parameter P_1 that is representing the maximal additional stress needed for unpinning and governed by the evolution of C_s that represents the relative concentration of solute atoms pinning the dislocations. C_s varies between 0 and 1 where $C_s = 1$ means that the dislocations are completely pinned whereas $C_s = 0$ corresponds to

a totally unpinned case. The parameters P_2 and α are driving the strain and time aging dependence of the pinning process. The parameter n is related to the pinning kinetics. The evolution of the aging time is defined in Eq. (7).

$$\dot{t}_a = 1 - \frac{\dot{p}}{\omega} t_a \quad ; \quad t_a(t=0) = t_{a0} \tag{7}$$

Where t_{a0} represents the initial aging time (to eventually account for pre-straining or aging) and ω that is associated with the incremental strain jump resulting from the transition of unpinned dislocations from one obstacle to another.

4. Identification of the temperature dependent parameters

4.1. *Identification procedure*

The identification of the parameters was done through the comparison of experimental and simulation results. It was done in two steps:

  (1) Volume element simulations to fit the overall hardening behavior and account for positive or negative strain rate sensitivity
  (2) 2D finite element simulations to verify if the parameters P_1, P_2, α that are controlling the propagation of the PLC band allow for a good agreement between the experimental 2D DIC results and the simulations

Those two steps were then iterated numerous times to reach a better agreement between the observed and simulated behavior.

4.2. *Parameter identification*

The constitutive equations presented above first depend on the viscoplastic parameters in the flow rule: $\dot{\varepsilon}_0$, E_a, V_a. Those parameters are identified with tensile tests where dynamic strain aging is not active (at 20 °C and 100 °C). The activation volume can be computed from the strain rate sensitivity coefficient S defined by Eq. (1) and computed at 4% strain:

$$V_a = \frac{k_b T}{E_a} \frac{1}{S} \tag{8}$$

The activation energy value was chosen to be 5×10^{-3} eV to correctly describe viscoplastic behavior at 20 °. The activation volume was then calculated for all the other temperature from Eq. (8) using the value of S experimentally observed at 20 °C. Thus, without strain aging in this model S would be constant across the temperature range under consideration, and it is the strain aging that accounts for the observed variation of S with temperature. The parameter $\dot{\varepsilon}_0$ was taken from [9] with a value of 10^{-7}.

Four parameters then appear in the strain hardening definition: R_0, Q, b and H. For each temperature R_0 was fixed manually. The other parameters Q, b, H were left to be numerically determined through the optimization process described below.

Lastly six parameters appear in the definition of the contribution of strain aging n, P_1, P_2, ω, α and t_{a0}. The parameter n is usually chosen to be equal to 0.66 or 0.33 corresponding to "bulk" or "pipe" propagation according to [20], the latter was chosen as it results in better agreement between the serrations produced by 2D FE calculations and the 2D DIC results. The parameter ω essentially influences the localization pattern in 3D and approaches an asymptotic value around 10^{-4} [21] so also that was chosen to be 10^{-4} by trial and error with 2D FE calculations for ω ranging from 10^{-3} to 10^{-4}, deciding based on improved agreement with the 2D DIC results. Since no Lüders behavior was observed at any temperature the parameter t_{a0} was fixed to 0 for all

the temperatures. Since it was not observed the identification of the strain aging parameters could not rely upon Lüders plateau characteristics like in other studies [5, 9, 22], as such the other parameters P_1, P_2 and α were left to be determined trough the optimization process.

Table 3. Temperature independent parameters of the KEMC model.

E_a(eV)	$\dot{\varepsilon}_0$(s^{-1})	n	ω	t_{a0}(s)	E(MPa)	ν
5×10^{-3}	10^{-7}	0,33	10^{-4}	0	168000	0.27

At this stage six parameters for each temperature remain to be identified: Q, b, H, P_1, P_2, α. The identification process was automated using a non linear least square optimization algorithm from the Scipy library of python [23]. For each temperature the experimental curves at both strain rates and volume element simulations obtained trough the integration of the constitutive equations with MFront [24] were compared in order to find an optimized set of parameters accounting for the overall behavior and the strain rate sensitivity.

The comparison between the volume element simulations with the optimized set of parameters and the experimental results are shown in Figure 7 for different temperatures. The final set of temperature-dependent parameters is presented in Table 4.
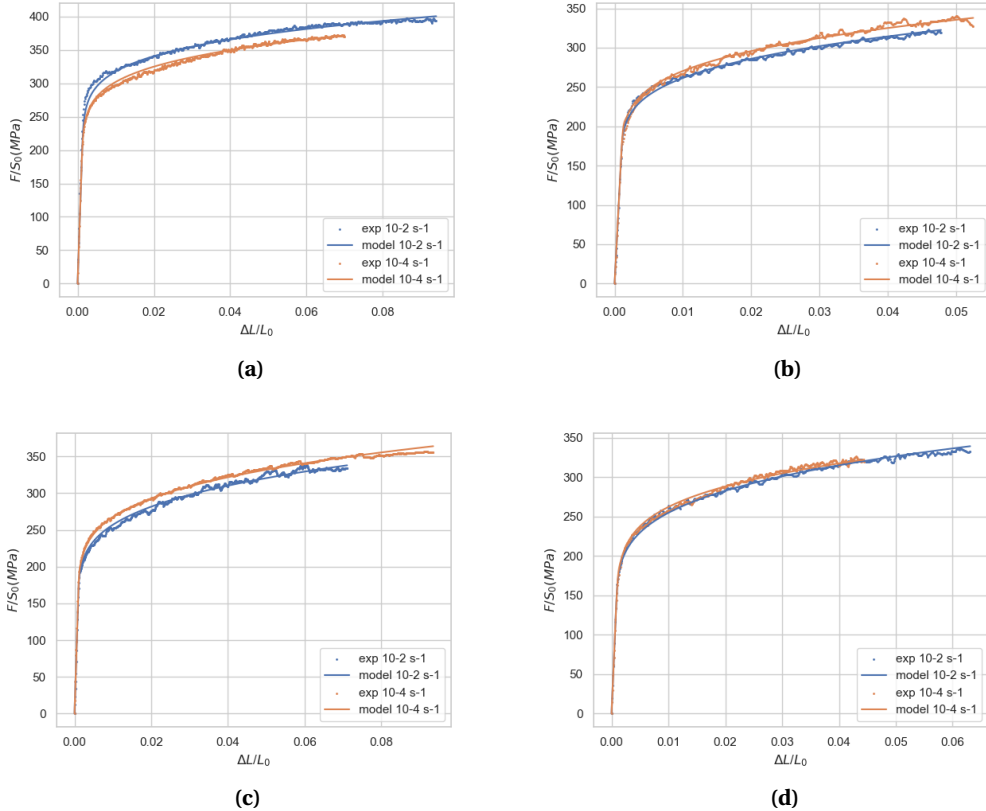

Figure 7. Volume element simulations with the optimized parameters and data at (a) 23°C, (b) 150°C, (c) 200°C and (d) 300°C.

For each temperature the difference of behavior between the two different strain rates is well captured. The choice of the power law hardening term allows a good fit when DSA is not active (Figure 7a) and the negative strain rate sensitivity is well captured in the 150-300 °C temperature range where DSA is active (Figures 7b, 7c, 7d). It is worth mentioning that no smoothing operation osn the experimental data was done to ease the optimization process.

Table 4. Temperature dependant parameters of the KEMC model.

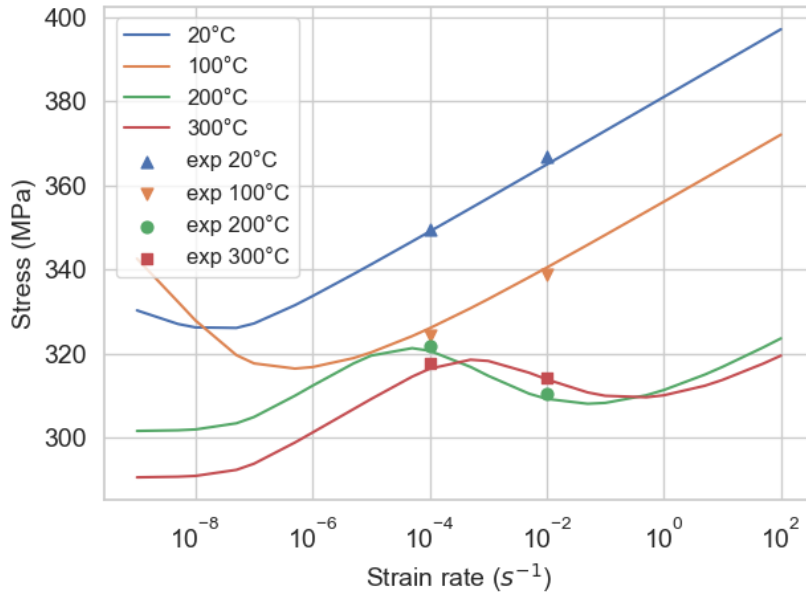|	20°C	100°C	150°C	200°C	300°C
R_0 (MPa)	118	110	105	100	90
Q (MPa)	354	370	360	353	373
b	0.17	0.21	0.26	0.27	0.27
H (MPa)	38	37.3	34.3	23.7	19.7
$V_a (10^{-30} \mathrm{m}^3)$	1153	1471	1670	1869	2267
P_1 (MPa)	56.9	56.4	56.4	54.1	47.8
$P_2 (\mathrm{s}^{-n})$	0.005	0.05	1.8	3.4	12.3
α	0.09	0.1	0.12	0.18	0.33

Figure 8. Predicted flow stress at 4% strain versus strain rate for 4 different temperatures and comparison with the experiments.

To have a better understanding of the chosen set of parameters presented in Tables 3 and 4 the predicted flow stress at 4 % strain for a wide range of stress rates and 4 different temperatures is shown in Figure 8. The flow stress is globally increasing with strain rate in between an intermediate domain of negative SRS for each temperature. This negative SRS behavior is a characteristic of the domain of PLC instabilities. The two positive SRS domains are corresponding to the classical viscosity of the material respectively for pinned dislocations (left side of the negative SRS domain) and unpinned dislocations (right side of the negative SRS domain). Different choices for

ϵ_0, V_a, and E_a can produce very similar simulation results, so not too much interpretation should be given to their precise values in terms of which physical mechanisms the model is accounting for. The values here are similar to those reported elsewhere for dynamic strain aging in steel.

The location of the experimental flow stresses at 4% strain on Figure 8 are in good agreement with the predicted behavior. The experimental points are also giving a good indication of whether serrations are to be expected in numerical simulations trying to reproduce the tests. If those points are located in the negative SRS domain then PLC should be active. As such simulations at 200°C for both strain rates and at 300°C for the faster strain rate are expected to produce serrations which is in good agreement with the experimental results.

5. Numerical modeling of tensile tests

The numerical modeling was carried within the Salomé Méca platform developed by EDF and the CEA. The constitutive equations were implemented into Code Aster [25] using MFront [24]. The behavior was integrated using an implicit scheme and the analytical jacobian matrix. The finite element resolution was then carried out using a Newton algorithm with the tangent matrix. 2D simulations were carried out to save computational resources. The simulations allowed to fine tune the parameters related to the band propagations and verify the behavior.

5.1. *2D simulations*

The simulations were carried in 2D using the plane stress assumption and the small strain framework as no rotations were expected. The mesh was generated using the transfinite algorithm of GMSH [26] and contained 300 8 node quadratic elements with reduced integration. The boundary conditions are visible in Figure 9, the displacement of the nodes of the left boundary were blocked along the x-direction, a displacement along the x-direction with velocity corresponding to the prescribed strain rate $\dot{E}$ was imposed for the nodes of the right boundary, and the rigid body motion was blocked by imposing no displacement along the y-direction for one node.
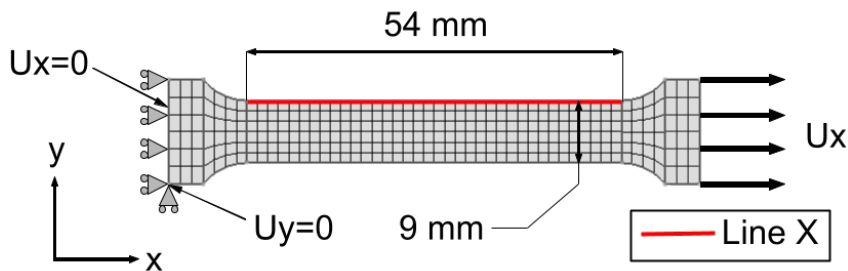

Figure 9. 2D mesh and the applied boundary conditions.

In order to compare the results of the 2D simulations and the experimental results the same type of procedure as in Figures 3, 4 and 5 was used to visualize the serrations. The value of $\dot{p}$ along line X (see Figure 9) was normalized with regards to the overall applied strain rate $\dot{E}$ and plotted in function of time. The results of the simulations for each combination of temperature and applied strain where PLC was clearly observed in the experiments are shown in Figures 10, 12, 14 and 16. For all the other combinations of temperature and applied strain the simulations did not produce any serrations and were equivalent to the volume element simulations (see Figure 7). The identified parameters are accurately producing serrations under the conditions where they

where observed in the experiments excepted for the end of the test at 300°C with a prescribed strain rate of $10^{-4}s^{-1}$.
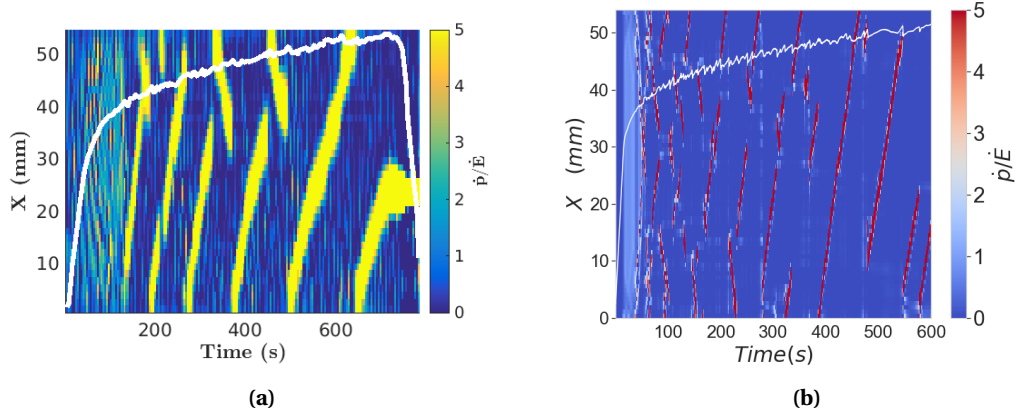

Figure 10. Spatio-temporal graphs of the experiments (left) and the simulations (right) at 150°C at $\dot{E} = 10^{-4}s^{-1}$.
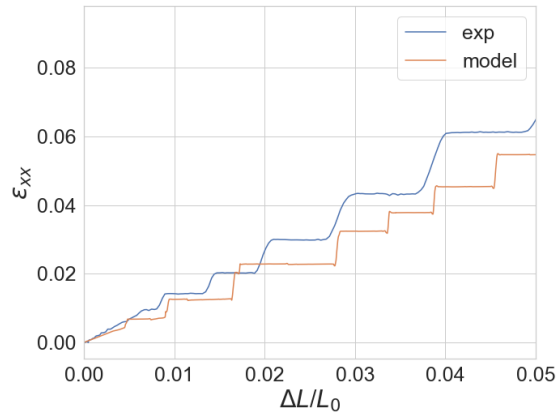

Figure 11. Local strain evolution at 150°C at $\dot{E} = 10^{-4}s^{-1}$.

Local strain jumps comparisons were also performed (Figures 11, 13, 15 and 17) by plotting the local strain ϵ_{xx} in the middle of the gauge length for the experiments and the 2D simulations. The amplitude and frequency of the simulated local strain jumps are overall in agreement with the experimental data. This overall agreement is to be attributed to the optimization of the parameters based on spatio-temporal graphs acquired using 2D DIC. The width of the local strain jumps is smaller in the simulations than in the measurements, but it is not clear whether this is a significant disparity. The microstructure of the cast iron and the measurement by DIC would tend to broaden these jumps in the experiment, whereas effects of discretisation in the finite element modeling may favour more sudden strain jumps. It is known that whereas the width of deformation bands in finite element modeling is mesh-dependent, the magnitude of the strain jumps is more reliably modelled [27]. It is clear that as an isotropic homogenous material model, the KEMC model is missing important features of the microstructure of cast iron, but it is able to capture many observed aspects of the deformation behavior.
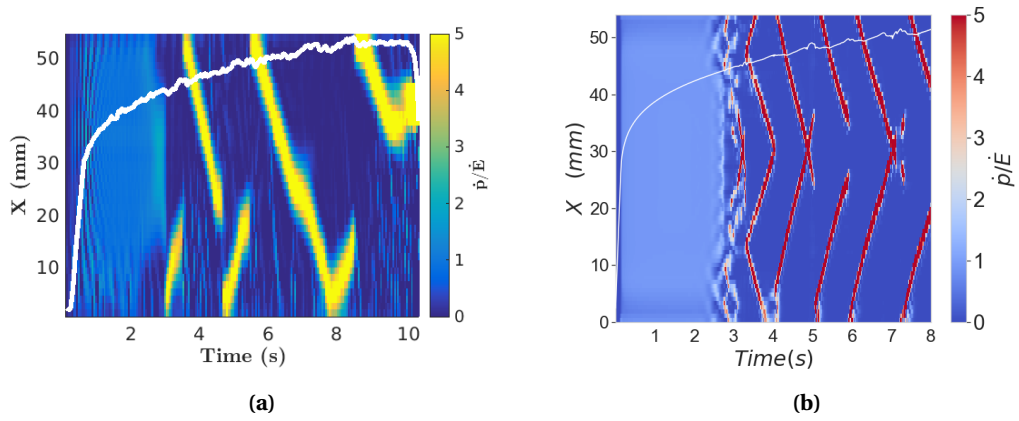
(a)   **(b)**

Figure 12. Spatio-temporal graphs of the experiments (left) and the simulations (right) at 200°C at $\dot{E} = 10^{-2} s^{-1}$.
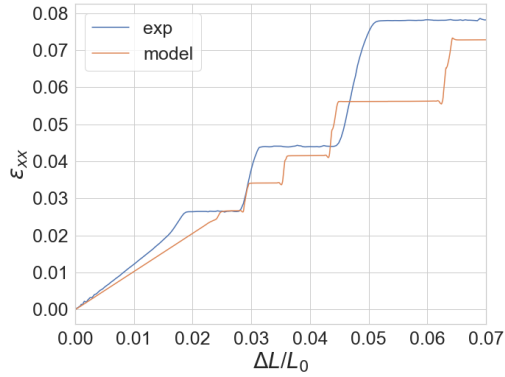

Figure 13. Local strain evolution at 200°C at $\dot{E} = 10^{-2} s^{-1}$.

(a)   **(b)**
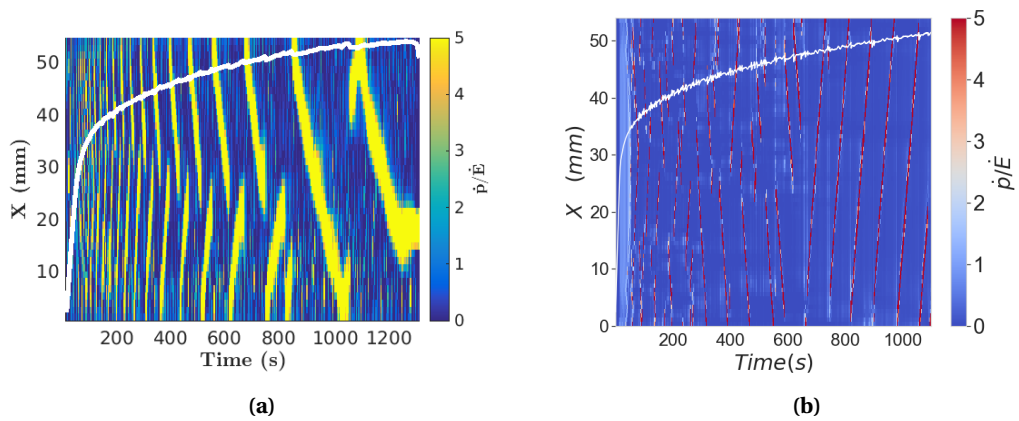
Figure 14. Spatio-temporal graphs of the experiments (left) and the simulations (right) at 200°C at $\dot{E} = 10^{-4} s^{-1}$.

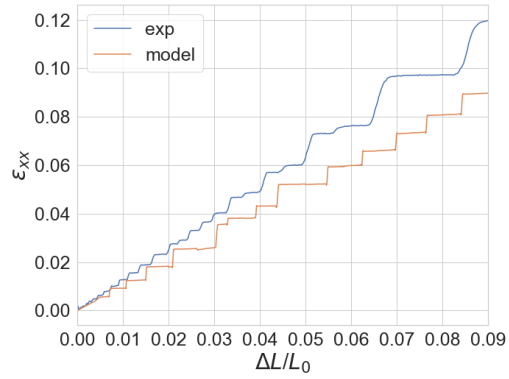**Figure 15.** Local strain evolution at 200°C at $\dot{E} = 10^{-4} s^{-1}$.
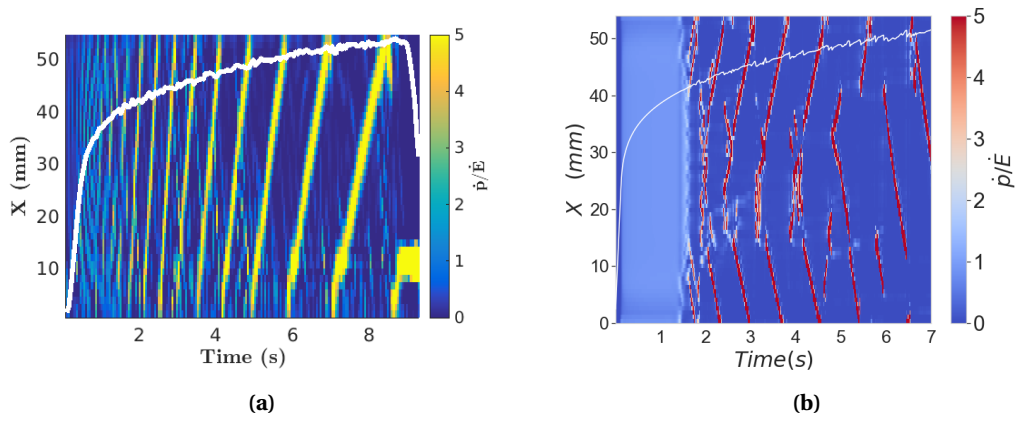

(a)

(b)

Figure 16. Spatio-temporal graphs of the experiments (left) and the simulations (right) at 300°C at $\dot{E} = 10^{-2} s^{-1}$.
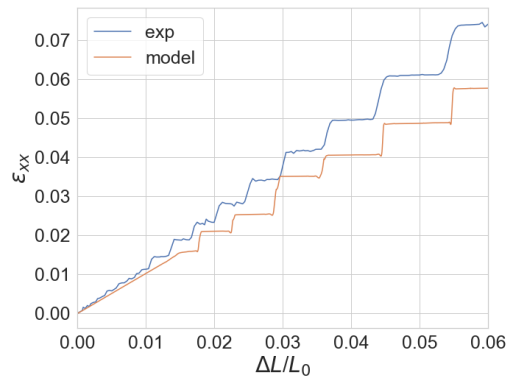

Figure 17. Local strain evolution at 300°C at $\dot{E} = 10^{-2} s^{-1}$.

6. Conclusion

Very few studies were conducted to analyse DSA in Ductile Cast Iron. In the present case, a series of tensile test was performed at temperatures ranging from 20° up to 300°at two different strain rates. The displacement fields were successfully measured and the strain localization patterns were observed. Such analyses were made possible by using 2D DIC.

A constitutive law based on the Kubin–Estrin–McCormick model (KEMC) was used to model the behavior of the ductile cast iron in temperatures ranging from 20° up to 300°. It is the first time that a model accounting for DSA is used for a Ductile Cast Iron. The measurements were used to calibrate the parameters of the constitutive law. Numerical simulations are shown to be in agreement with experimental measurements at the macroscopic scale.

The study presented herein calls for further experiments. Considering the well-known differences between tensile and compressive deformation in cast iron, whether DSA is also active in compression should be investigated. Moreover, especially for the use of this material in a long-term geological repository, it would be interesting to expand the experimental data set with measurements at even lower strain rates and at different temperatures. Lastly it would be of interest to assess the interaction between DSA and hydrogen embrittlement [28], since the easy diffusion of the small hydrogen atoms may be expected to affect the interaction of other interstitial atoms with dislocations, and therefore affect both the energetics and the kinetics of the formation of Cotterell clouds believed to be responsible for dynamic strain aging.

Declaration of interests

The authors do not work for, advise, own shares in, or receive funds from any organization that could benefit from this article, and have declared no affiliations other than their research organizations.

Acknowledgments

Appendix: 2D DIC hardware and analyses parameters

Table 5. 2D DIC hardware parameters

Detector	Basler ace acA4096-40um
Definition	4096 × 2168 pixels
Gray Levels amplitude	10-12 bits
Objective	Hikvision
Focal length	50 mm
Physical size of a pixel	0.03 mm

Table 6. 2D DIC analysis parameters

2D DIC software	Correli 3.0 [18]
Image filtering	none
Element length (mean)	29 px
Shape functions	linear (T3 elements [29])
Mesh	see Figure 2
Matching criterion	penalized sum of squared differences
Regularization length	$\ell_m = 50$ px
Interpolant	cubic
Displacement noise floor	0.022 / 0.008 px
Strain noise floor	1.3×10^{-4} / 1.4×10^{-4}
Estimated 2D parallax error (at 10%)	1×10^{-4}

References

[1] P. Minnebo, K. Nilsson, D. Blagoeva, "Tensile, Compression and Fracture Properties of Thick-Walled Ductile Cast Iron Components.", *J. Mater. Eng. Perform.* **16** (2007), p. 35-45.

[2] K. Nilsson, P. Dillström, C. G. Andersson, F. Nilsson, M. Andersson, P. Minnebo, L. E. Björkegren, B. Erixon, "A Probabilistic Methodology to Determine Failure Probabilities and Acceptance Criteria for the KBS-3 Inserts Under Ice-Age Load Conditions", *Nucl. Technol.* **163** (2008), p. 3-14.

[3] Z. Jiang, Q. Zhang, H. Jiang, Z. Chen, X. Wu, "Spatial characteristics of the Portevin–Le Chatelier deformation bands in Al-4at%Cu polycrystals", *Mater. Sci. Eng. A* **403** (2005), p. 154-164.

[4] T. Böhlke, G. Bondár, Y. Estrin, M. A. Lebyodkin, "Geometrically non-linear modeling of the Portevin–Le Chatelier effect", *Comput. Mater. Sci.* **44** (2009), p. 1076-1088.

[5] S. C. Ren, T. F. Morgeneyer, M. Mazière, S. Forest, G. Rousselier, "Portevin–Le Chatelier effect triggered by complex loading paths in an Al–Cu aluminium alloy", *Philos. Mag.* **99** (2019), p. 659-678.

[6] H. Halim, D. Wilkinson, M. Niewczas, "The Portevin–Le Chatelier (PLC) effect and shear band formation in an AA5754 alloy", *Acta Mater.* **55** (2007), p. 4151-4160.

[7] R. C. Picu, G. Vincze, F. Ozturk, J. J. Gracio, F. Barlat, A. M. Maniatty, "Strain rate sensitivity of the commercial aluminum alloy AA5182-O", *Mater. Sci. Eng. A* **390** (2005), p. 334-343.

[8] H. Louche, P. Vacher, R. Arrieux, "Thermal observations associated with the Portevin–Le Châtelier effect in an Al–Mg alloy", *Mater. Sci. Eng. A* **404** (2005), p. 188-196.

[9] J. Belotteau, C. Berdin, S. Forest, A. Parrot, C. Prioul, "Mechanical Behavior and Crack Tip Plasticity of a Strain Aging Sensitive Steel", *Mater. Sci. Eng. A* **526** (2009), p. 156-165.

[10] H. D. Wang, C. Berdin, M. Mazière, S. Forest, C. Prioul, A. Parrot, P. Le-Delliou, "Experimental and numerical study of dynamic strain ageing and its relation to ductile fracture of a C–Mn steel", *Mater. Sci. Eng. As* **547** (2012), p. 19-31.

[11] L. Fournier, D. Delafosse, T. Magnin, "Oxidation induced intergranular cracking and Portevin–Le Chatelier effect in nickel base superalloy 718", *Mater. Sci. Eng. A* **316** (2001), p. 166-173.

[12] K. B. S. Rao, S. Kalluri, G. R. Halford, M. A. McGaw, "Serrated flow and deformation substructure at room temperature in Inconel 718 superalloy during strain controlled fatigue", *Scripta Metallurgica et Materialia* **32** (1995), p. 493-498.

[13] K. Prasad, S. V. Kamat, "Transient flow behaviour in a near alpha titanium alloy Timetal 834 in the dynamic strain aging regime", *Mater. Sci. Eng. A* **490** (2008), p. 477-480.

[14] P. G. McCormick, "Theory of flow localisation due to dynamic strain ageing", *Acta Metallurgica* **36** (1988), p. 3061-3067.

[15] L. P. Kubin, Y. Estrin, "The Portevin–Le Chatelier effect in deformation with constant stress rate", *Acta Metallurgica* **33** (1985), p. 397-407.

[16] Y. Estrin, P. G. McCormick, "Modelling the transient flow behaviour of dynamic strain ageing materials", *Acta Met. Mater.* **39** (1991), p. 2977-2983.

[17] V. Björklund, "The effects of static strain aging on the mechanical performance of nodular cast iron", PhD Thesis, Aalto University. School of Engineering, 2021, Master's thesis, http://urn.fi/urn:nbn:fi:aalto-202109059026, 104 pages.

[18] H. Leclerc, J. Neggers, F. Mathieu, F. Hild, S. Roux, "Correli 3.0 IDDN.FR.001.520008.000.S.P.2015.000.31500", Tech. report, Agence pour la Protection des Programmes, Paris (France), 2015.

[19] S. Zhang, P. G. McCormick, Y. Estrin, "The Morphology of Portevin–Le Chatelier Bands: Finite Element Simulation for Al–Mg–Si", *Acta Mater.* **49** (2001), p. 1087-1094.

[20] F. Springer, C. Schwink, "Quantitative investigations on dynamic strain ageing in polycrystalline CuMn alloys", *Scripta Metallurgica et Materialia* **25** (1991), no. 12, p. 2739-2744.

[21] H. Wang, C. Berdin, M. Mazière, S. Forest, C. Prioul, A. Parrot, P. Le-Delliou, "Portevin–Le Chatelier (PLC) instabilities and slant fracture in C–Mn steel round tensile specimens", *Scr. Mater.* **64** (2011), no. 5, p. 430-433.

[22] A. Marais, M. Mazière, S. Forest, A. Parrot, P. L. Delliou, "Identification of a strain-aging model accounting for Lüders behavior in a C-Mn steel", *Philos. Mag.* **92** (2012), no. 28-30, p. 3589-3617.

[23] P. Virtanen, R. Gommers, T. E. Oliphant, M. Haberland, T. Reddy, D. Cournapeau, E. Burovski, P. Peterson, W. Weckesser, J. Bright, S. J. van der Walt, M. Brett, J. Wilson, K. J. Millman, N. Mayorov, A. R. J. Nelson, E. Jones, R. Kern, E. Larson, C. J. Carey, İ. Polat, Y. Feng, E. W. Moore, J. VanderPlas, D. Laxalde, J. Perktold, R. Cimrman, I. Henriksen, E. A. Quintero, C. R. Harris, A. M. Archibald, A. H. Ribeiro, F. Pedregosa, P. van Mulbregt, SciPy 1.0 Contributors, "SciPy 1.0: Fundamental Algorithms for Scientific Computing in Python", *Nat. Methods* **17** (2020), p. 261-272.

[24] T. Helfer, B. Michel, J.-M. Proix, M. Salvo, J. Sercombe, M. Casella, "Introducing the open-source mfront code generator: Application to mechanical behaviours and material knowledge management within the PLEIADES fuel element modelling platform", *Comput. Math. Appl.* **70** (2015), no. 5, p. 994-1023.

[25] Electricité de France, "Finite element *code_aster*, Analysis of Structures and Thermomechanics for Studies and Research", 1989–2022, Open source on www.code-aster.org.

[26] C. Geuzaine, J.-F. Remacle, "Gmsh: a three-dimensional finite element mesh generator with built-in pre- and post-processing facilities", *Int. J. Numer. Methods Eng.* **79** (2009), p. 1309-1331.

[27] M. Mazière, J. Besson, S. Forest, B. Tanguy, H. Chalons, F. Vogel, "Numerical aspects in the finite element simulation of the Portevin–Le Chatelier effect", *Comput. Methods Appl. Mech. Eng.* **199** (2010), p. 734-754.

[28] P. Sahiluoma, Y. Yagodzinskyy, A. Forsström, H. Hänninen, S. Bossuyt, "Hydrogen Embrittlement of Nodular Cast Iron", *Mater. Corros. - Werkst. Korros.* **72** (2021), p. 245-254.

[29] F. Hild, A. Bouterf, L. Chamoin, F. Mathieu, J. Neggers, F. Pled, Z. Tomičević, S. Roux, "Toward 4D Mechanical Correlation", *Adv. Model. and Simul. in Eng. Sci.* **3** (2016), no. 1, p. 1-26.